Lin et al. Nanoscale Research Letters (2015) 10:446
DOI 10.1186/s11671-015-1156-0

Nanoscale Research Letters
a SpringerOpen Journal

NANO EXPRESS Open Access

# Low-Temperature Thermally Reduced Molybdenum Disulfide as a Pt-Free Counter Electrode for Dye-Sensitized Solar Cells

Che-Hsien Lin[1], Chuen-Horng Tsai[1], Fan-Gang Tseng[1*], Yang-Yen Yu[2], Hsuan-Chung Wu[2] and Chien-Kuo Hsieh[2*]

**Abstract**

A two-dimensional nanostructure of molybdenum disulfide ($MoS_2$) thin film exposed layered nanosheet was prepared by a low-temperature thermally reduced (TR) method on a fluorine-doped tin oxide (FTO) glass substrate as a platinum (Pt)-free and highly electrocatalytic counter electrode (CE) for dye-sensitized solar cells (DSSCs). Thermogravimetric analysis (TGA) results show that the $MoS_2$ sulfidization temperature was approximately 300 °C. X-ray photoelectron spectroscopy (XPS), high-resolution transmission electron microscopy (HRTEM), and X-ray diffraction (XRD) indicate that the stoichiometry and crystallization of $MoS_2$ were more complete at higher temperatures; however, these temperatures reduce the number of edge-plane active sites in the short-range-order nanostructure. Accordingly, the DSSCs with 300 °C annealed TR-$MoS_2$ CE exhibited an excellent photovoltaic conversion efficiency (PCE) of 6.351 %, up to 91.7 % of which is obtained using the conventional TD-Pt CE (PCE = 6.929 %). The temperature of thermal reaction and the molar ratio of reaction precursors were found to significantly influence the resulting stoichiometry and crystallization of $MoS_2$ nanosheets, thus affecting DSSCs' performance.

**Keywords:** Molybdenum disulfide, Thermal reduction, Counter electrode, Dye-sensitized solar cells

## Background

Since the first demonstration of dye-sensitized solar cells (DSSCs) by O'Regan and Grätzel [1], much attention has been paid to these third-generation solar cells due to their low cost, easy fabrication, high photo conversion efficiency, and environmental friendliness [2–5]. A DSSC typically comprises of a wide-band semiconductor (usually $TiO_2$) coated with dye molecules on a transparent conductive glass as a working electrode (WE), an electrolyte-containing iodide/triiodide ($I^-/I_3^-$) redox couple, and a counter electrode (CE), usually deposited platinum (Pt) on the transparent conductive glass. Pt is conventionally used as the CE catalyst in DSSCs to regenerate the electrolyte redox couple and collect electrons to complete the circuit. However, because the high cost and scarcity of Pt greatly restrict the commercial production of DSSCs, the development of low-cost, good electrical conductivity, and high-electrocatalyst CE materials is highly desired to provide an economic solution for high-performance DSSCs.

Stimulated by the outstanding electrochemical activity of graphene, two-dimensional (2D) nanomaterials have attracted great attention in recent years [5–8]. Transition metal dichalcogenides (TMDCs), $MX_2$, (M = Nb, Ta, Mo, W; X = S, Se, Te), have received much interest due to their 2D layered nanostructures, which are analogous to the graphene structure [9–11]. As a typical TMDC, the layer-dependent properties of molybdenum disulfide ($MoS_2$) have recently attracted considerable attention due to their great potential in the electrochemical fields of catalysis [9, 12], lithium-ion batteries [13–15], hydrogen evolution [9, 16, 17], and DSSCs [18, 19]. $MoS_2$ is composed of three stacked atomic layers (a Mo layer sandwiched between two S layers, S–Mo–S) and held together through van der Walls interactions [20].

However, $MoS_2$ tends to form zero-dimensional fullerene-like nanoparticles or one-dimensional nanotubes

* Correspondence: fangangtseng@gmail.com; jack_hsieh@mail.mcut.edu.tw
[1]Department of Engineering and System Science, National Tsing Hua University, Hsinchu 30013, Taiwan, Republic of China
[2]Department of Materials Engineering, Ming Chi University of Technology, 84 Gungjuan Rd., Taishan District, New Taipei City 24301, Taiwan, Republic of China

during the synthetic process [21, 22]. Therefore, an efficient way to synthesize 2D layer-nanostructured $MoS_2$ is to use graphene or carbon nanotubes (CNTs) as a template substrate [10, 16, 18, 23]. Although significant efforts have been devoted to the preparation of 2D layer-nanostructured $MoS_2$, including scotch tape-based micromechanical exfoliation [24], liquid exfoliation [25–28], hydrothermal synthesis [14, 29], physical vapor deposition [30, 31], and chemical vapor deposition [32, 33], the easy synthesis of 2D layer-nanostructured $MoS_2$ at low temperatures by template-free approaches under mild conditions still remains a challenge [34, 35]. Additionally, the electrochemical activities of $MoS_2$ were correlated with the number of catalytically active edge sites [9, 12, 17, 36], for the reason that controlling the nanostructures with more edge sites at the atomic scale is an effective strategy to gain an effective $MoS_2$ catalyst. In this study, we produce an easy, thermally reduced (TR) $MoS_2$ nanosheet thin film on fluorine-doped tin oxide (FTO) glass at low temperature that provides the number of edge-plane active sites in the short-range-order nanostructure of $MoS_2$ nanosheets, and demonstrates good catalytic performance compared with conventional Pt CE DSSCs.

## Methods

### Preparations of the Molybdenum Disulfide Counter Electrodes

A FTO transparent glass (TEC-7, 2.2 mm, Hartford) substrate was ultrasonically cleaned sequentially in detergent, acetone (overnight), distilled water (DI water, 1 h), and ethanol (1 h). Ammonium tetrathiomolybdate ($(NH_4)_2MoS_4$) powder (ProChem Inc., 99.99 % purity; 0.8 g) was added to 20 mL of N,N-dimethylformide (DMF) to form a 4 wt% solution. The solution was then sonicated for 1 day before use [28]. Furthermore, the dispersed solution was coated on FTO glass by spin coating at 1600 rpm to control the thickness and flatness of the film. The substrate was then dried in air for 1 h and annealed in an $H_2/Ar = 1:9$ gas mixture at various temperatures for 45 min to obtain thermally reduced molybdenum sulfide (TR-$MoS_x$) samples. The annealing temperatures for the $MoS_2$ phase transformation in this study are 250, 300, and 350 °C. The thermally deposited platinum (TD-Pt) CE was prepared as a reference electrode by thermal reduction, which was carried out by dropping a $H_2PtCl_6$ isopropanol solution on an FTO glass substrate annealed at 450 °C for 20 min [37].

### Fabrication of the $TiO_2$ Working Electrode

The working electrode utilized the same FTO glass coated with nanocrystalline $TiO_2$ using the print-screen method; the area and thickness of the $TiO_2$ film were about 0.28 $cm^2$ and 10 μm, respectively. The $TiO_2$ WE was then gradually sintered to 550 °C in ambient air for 30 min before being slowly cooled at room temperature (RT). After calcination, the $TiO_2$ WE was then immersed in a N719 (Solaronix) solution ($3 \times 10^{-3}$ M in a 1:1 volumetric mixture of acetonitrile and *tert*-Butylalcohol) at RT for 24 h. Following the dye adsorption process, the dye-adsorbed $TiO_2$ WE was washed with acetonitrile to remove the remaining dye and dried at RT for a few seconds.

### Fabrication of DSSC Devices

The efficiency of the TR-$MoS_x$ CEs as well as the standard TD-Pt CE DSSC devices were quantitatively compared. The dye-adsorbed $TiO_2$ WE was future assembled with a CE into a sandwiched configuration and sealed with a 60-μm hot-melt surlyn (SX1170-60, Solaronix) by heating at 100 °C for a few seconds. The DSSC device was fabricated by drilling two holes on the CE and injecting an iodide-based electrolyte (AN-50, Solaronix) in the space between the electrodes after the assembling process. Finally, the holes on the CE were sealed after the electrolyte injection. DSSC devices were then illuminated by a class A quality solar simulator with a light intensity of 100 mW $cm^{-2}$ (AM 1.5), which was calibrated with a standard silicon cell.

### Characterizations of Molybdenum Sulfide Counter Electrodes

In order to investigate the phase transformation and chemical states of the low-temperature thermally reduced $MoS_2$, thermogravimetric analysis (TGA) was conducted using a thermogravimetric analyzer (TGA Q50 V20.10 Build 36, USA) with a heating rate of 5 °C $min^{-1}$ in ambient Nitrogen. X-ray photoelectron spectroscopy (XPS) was conducted using a PHI Quantera SXM/AES 650 (ULVAC-PHI INC., Japan.) equipment with a hemispherical electron analyzer and a scanning monochromated Al Kα (hv = 1486.6 eV) X-ray source to study the chemical states of Mo and S of the prepared $MoS_x$ annealing samples. The XPS curve-fitting program, XPSPEAK 4.1, was used for peak de-convolution and assignment of binding energies, which was referenced to the adventitious C1s peak at 284.6 eV. For spectrum analysis, the background signal was subtracted by Shirley's method, and the curve fitting was performed by using a Gaussian–Lorentzian peak after Shirley background correction. Raman spectra were collected with a confocal micro-Raman spectroscopy (LABRAM HR 800 UV, Japan) using a 514-nm $Ar^+$ laser source with a spot size of approximately 1 μm. The surface morphology of the prepared $MoS_x$ annealing samples was examined by using the field emission scanning electron microscope (FESEM, JEOL, JSM-6330F, Japan). The nanostructures of $MoS_2$ were examined by using the transmission electron microscope (TEM, JEOL-2100F, Japan) equipped with EDS to determine the elements

contained in the samples. X-ray diffraction (XRD, PANalytical-X'Pert PRO MPD) with a CuKα radiation of 0.1541 nm was used to determine the crystallinities of the films.

According to our previous studies [3, 4], cyclic voltammetry (CV) measurements and the electrochemical impedance spectroscopy (EIS) were carried out to examine electrochemical properties. CV measurements were used to measure electrochemical redox ability using a potentiostat/galvanostat (PGSTAT 302N, Autolab, Eco Chemie, Netherlands) in a three-electrode configuration. Platinum wire and an Ag/AgCl electrode were used as the counter and reference electrodes, respectively. The solution used for CV measurements contained 1 mM $I_2$, 10 mM LiI, and 0.1 M $LiClO_4$ in acetonitrile. EIS spectra were obtained using the aforementioned potentiostat/galvanostat equipped with a frequency response analysis (FRA) module; EIS results were analyzed using an equivalent circuit model with Autolab FRA software (v4.9, EcoChemie B.V.). The frequencies used in the scan ranged from $10^6$ to $10^{-2}$ Hz, and an applied voltage of 10 mV was used.

In addition, Tafel polarization measurements were carried out using the potentiostat/galvanostat equipped with a linear polarization module to examine the electrocatalytic activity at the electrolyte–electrode interface. Both EIS and Tafel polarization measurements were obtained using symmetrical devices in the dark.

The photocurrent–voltage characteristics of DSSC devices were measured under simulated solar illumination (AM 1.5, 100 mW $cm^{-2}$, Oriel 91160, Newport Corporation, USA), equipped with an AM 1.5G filter (Oriel 81088A, Newport Corporation, USA) and a 300-W xenon lamp (Oriel 6258, Newport Corporation, USA). The simulated incident light intensity was calibrated using a reference Si cell (calibrated at NREL, PVM-81).

## Results and Discussion

### Composition and Morphologies

In this study, our homemade CVD system served as an important tool for the TR-$MoS_x$ annealing at low temperatures. TGA curves for the three complexes, $(NH_4)_2MoS_4$, 4 wt% $(NH_4)_2MoS_4$ in DMF, and pure $MoS_2$ powder, as shown in Fig. 1, were analyzed to identify the $MoS_2$ sulfidization temperature region. Quantitative data derived from the TGA curves are summarized in Table 1. As we can see from curve (a) in Fig. 1, the $(NH_4)_2MoS_4$ monomer decomposition was similar to a previous report [38]; there are two TGA regions in curve (a). The first is a sharp step from RT to 200 °C that corresponds to the loss of ammonia and hydrogen sulfide according to the following reaction:

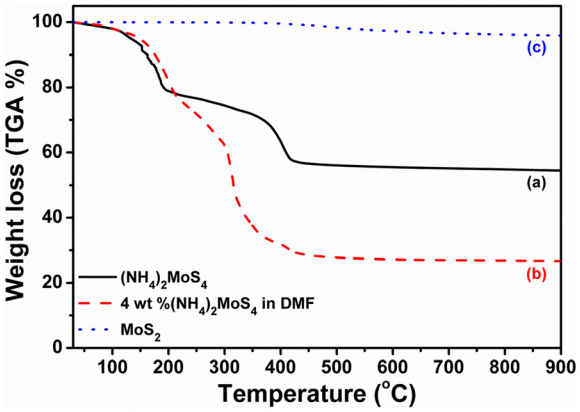


**Fig. 1** Thermogravimetric analysis (TGA) curves at 5 °C $min^{-1}$ for the thermal decomposition in $N_2$ atmosphere of (*a*) $(NH_4)_2MoS_4$, (*b*) $(NH_4)_2MoS_4$ dispersed in DMF, and (*c*) $MoS_2$ powder

$$(NH_4)_2MoS_4 \rightarrow 2NH_3 + H_2S + MoS_3 \quad (1)$$

The second decomposition occurs from 200 to 420 °C, indicating the $MoS_2$ phase transformation according to Eq.(2).

$$MoS_3 + H \rightarrow MoS_2 + H_2S \quad (2)$$

The $(NH_4)_2MoS_4$ precursor dispersed in DMF was also analyzed by TGA (curve (b) in Fig. 1); the most weight loss occurs in the temperature range from 220 °C to 450 °C, which also indicates the $MoS_2$ phase transformation. Commercial $MoS_2$ powder was also used as a reference (curve (c) in Fig. 1) that shows a broad temperature region (RT to 900 °C) and great thermal stability [39]. For future study, we carried out the three annealing conditions in our homemade furnace thermal CVD in $H_2$ mixed gas ($H_2$/Ar = 1:9) at 350, 300, and 250 °C.

In this study, we focused on the non-stoichiometric chemical compositions of TR-$MoS_x$ thin films in different temperature regions; the relationship of temperature with the performance was studied by XPS at various temperatures. Figure 2 shows the XPS spectrum of the TR-$MoS_x$ samples annealed at 350, 300, and 250 °C; the left side and right side of Fig. 2 show the chemical states of Mo 3d and S 2p orbitals, respectively. The peak positions, intensities (atomic percentage), and the stoichiometric ratio (S/Mo) are also given in Table 2.

The TR-$MoS_x$ annealed at 350 °C exhibits two main peaks of Mo 3d spectra at 229.22 and 232.36 eV that correspond to $Mo^{4+}$ $3d_{5/2}$ and $Mo^{4+}$ $3d_{3/2}$ orbitals, revealing that the $Mo^{4+}$ state is dominant in the 350 °C annealed sample and indicating the formation of $MoS_2$ [12]. Additional peaks are observed at 162.05 and 163.24 eV, which correspond to the known S $2p^{2-}{}_{3/2}$ and S $2p^{2-}{}_{1/2}$ $MoS_2$ doublet peaks, respectively [12].

**Table 1** Thermal analysis data for the thiomolybdates decomposition in $N_2$

| Compound | TG region | Temperature range (°C) | Probable product | Experimental weight loss (%) |
|---|---|---|---|---|
| $(NH_4)_2MoS_4$ | 1 | RT –200 | $MoS_3$ | 21.08 |
| | 2 | 200–900 | $MoS_2$ | 45.50 |
| $(NH_4)_2MoS_4$ + DMF | 1 | RT –225 | $MoS_3$(+DMF) | 24.51 |
| | 2 | 225–900 | $MoS_2$ | 73.31 |
| $MoS_2$ | 1 | RT –900 | $MoS_2$ | <1 |

The stoichiometric ratio (S/Mo) quantified by relative sensitivity factors (RSF) from the respective integrated peak area of XPS spectra is close to 2.03, also indicating that the structure of the 350 °C annealed sample is $MoS_2$. Whereas the annealing temperature is lowered to 250 °C, in addition to that the XPS peaks of the $MoS_2$ structure, other deconvoluted peaks need the concern. The peaks at 230.18 eV ($Mo^{5+}$ $3d_{5/2}$) and 233.32 eV ($Mo^{5+}$ $3d_{3/2}$), 231.40 eV ($Mo^{6+}$ $3d_{5/2}$) and 234.54 eV ($Mo^{6+}$ $3d_{3/2}$), 232.50 eV ($Mo^{6+}$ $3d_{5/2}$) and 235.64 eV ($Mo^{6+}$ $3d_{3/2}$), representing the Mo $3d_{5/2}$ and Mo $3d_{3/2}$ of the three valence states can be assigned to $Mo_2S_5$, $MoS_3$, and $MoO_3$, respectively [12, 40, 41]. Meanwhile, the binding energy at 163.20 eV ($S_2^{2-}$ $2p_{3/2}$) and 164.39 eV ($S_2^{2-}$ $2p_{1/2}$) might represent to the intermediate product of $Mo_2S_5$ and the $MoS_3$ with a formula of $[Mo^{4+}(S_2)^{2-}S^{2-}]$ [42, 43]. It is worthwhile to mention that the $MoS_2$ fraction decrement is nearly linear with annealing temperature down to 250 °C, and it becomes gradual at lower temperatures. These results suggest an incomplete $MoS_2$ phase transformation at lower annealing temperature, which is consistent with our TGA results. The stoichiometric ratio (S/Mo) estimated from the 250 and 300 °C annealing sample were 2.26 and 2.19, respectively. In addition, compared with the 250 °C annealing sample, note that the line width of $MoS_2$ peaks becomes progressively stronger and narrower for annealing temperatures above 300 °C.

The Raman spectrums of the synthesized samples are shown in Fig. 3. All annealing samples showed the two

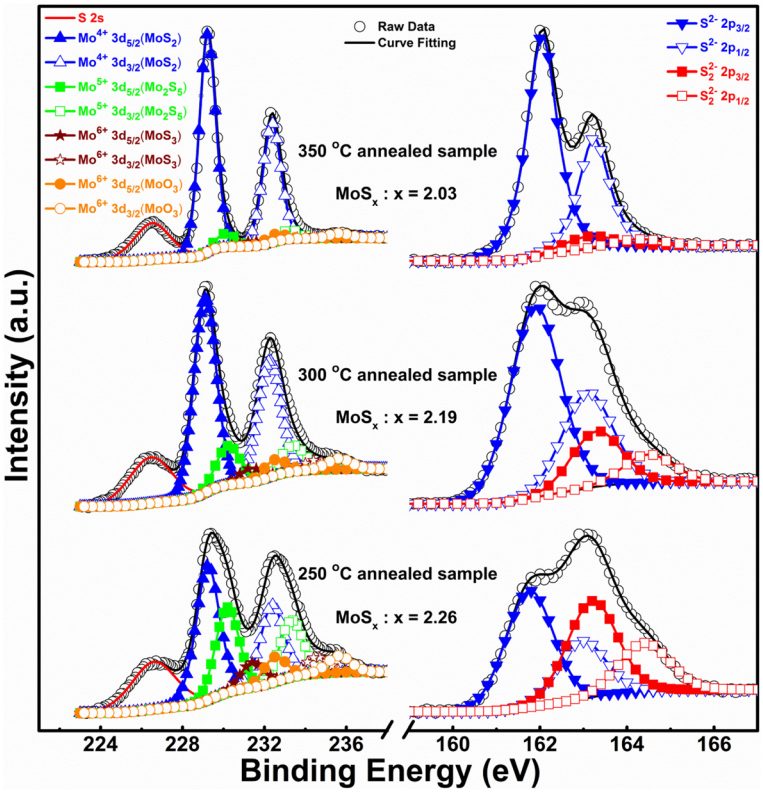


**Fig. 2** The Mo 3d and S 2p peak in the XPS spectra of the TR-$MoS_x$ annealed at 350, 300, and 250 °C

**Table 2** The Mo 3d and S 2p peak positions, atomic percentages, and *x* values of the TR-$MoS_x$ samples annealed at 250, 300, and 350 °C

| Peak and identity | | Fitting of Mo 3d and S 2p peak binding energy (eV) (atomic percentage (%)) | | |
|---|---|---|---|---|
| | | 250 °C | 300 °C | 350 °C |
| $Mo^{4+}$ $3d_{5/2}$ | $MoS_2$ | 229.23(31.2) | 229.10(44.4) | 229.22(54.0) |
| $Mo^{4+}$ $3d_{3/2}$ | | 232.37(18.1) | 232.24(27.6) | 232.36(32.6) |
| $Mo^{5+}$ $3d_{5/2}$ | $Mo_2S_5$ | 230.18(19.2) | 230.23(9.7) | 230.10(4.2) |
| $Mo^{5+}$ $3d_{3/2}$ | | 233.32(12.8) | 233.37(6.4) | 233.24(2.8) |
| $Mo^{6+}$ $3d_{5/2}$ | $MoS_3$ | 231.40(5.6) | 231.30(3.4) | 231.40(1.7) |
| $Mo^{6+}$ $3d_{3/2}$ | | 234.54(3.8) | 234.44(2.3) | 234.54(1.1) |
| $Mo^{6+}$ $3d_{5/2}$ | $MoO_3$ | 232.50(5.6) | 232.50(3.7) | 232.50(2.2) |
| $Mo^{6+}$ $3d_{3/2}$ | | 235.64(3.8) | 235.64(2.5) | 235.64(1.5) |
| $S^{2-}$ $2p_{3/2}$ | $MoS_2$ | 161.76(35.7) | 161.90(51.8) | 162.05(61.7) |
| $S^{2-}$ $2p_{1/2}$ | | 162.95(17.9) | 163.09(25.9) | 163.24(30.9) |
| $S_2^{2-}$ $2p_{3/2}$ | – | 163.20(30.9) | 163.30(14.9) | 163.10(4.9) |
| $S_2^{2-}$ $2p_{1/2}$ | | 164.39(15.5) | 164.49(7.4) | 164.29(2.5) |
| S/Mo ratio (*x* values) | | 2.26 | 2.19 | 2.03 |

prominent Raman peaks of $MoS_2$ at about 381 $cm^{-1}$ ($E^1_{2g}$) and 406 $cm^{-1}$ ($A_{1g}$) [44]. The $E^1_{2g}$ mode corresponds to the in-plane vibration from two S atoms with respect to the Mo atom in opposite vibration; the $A_{1g}$ mode is associated with the out-of-plane vibration of only S atoms along the plane directions [45]. In addition, the observation of $E^1_{2g}$ and $A_{1g}$ Raman peaks at 381 and 406 $cm^{-1}$ suggested the presence of multi-layered $MoS_2$ nanosheets [44, 45]. Meanwhile, the peak intensity and full width at half maximum (FWHM) of $MoS_2$ becomes stronger and narrower as the annealing temperature up to 300 °C, that suggested the complete and genuine $MoS_2$ structure.

Figure 4 shows the SEM images that correspond to the bare FTO substrate and the TR-MoSx samples annealed at 250, 300, and 350, respectively. Obviously, all the prepared TR-MoSx electrodes showed the film-like morphology on the surface of FTO substrate, which was prepared by spin coating technology and controlled the flatness of the film.

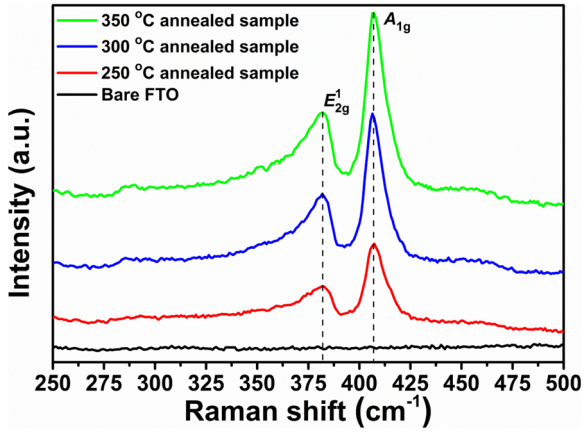


**Fig. 3** Raman spectra of TR-$MoS_x$ samples annealed at various temperatures recorded using a 514-nm excitation wavelength

Figure 5 shows high-resolution transmission electron microscopy (HRTEM) images and the corresponding selected area electron diffraction (SAED) of the annealed samples at 250, 300, and 350 °C. Figure 5a, d shows the HRTEM image and SAED of the $MoS_x$ annealed at 250 °C, respectively. Because the major phase is $MoS_3$ at 250 °C, we can confirm that the $MoS_3$ synthesized at this temperature is noncrystalline, which is consistent with a previous report [18]. Fig. 5b shows the separated layer-nanostructured $MoS_2$, formed after the $MoS_3$ was converted to crystallized $MoS_2$ at 300 °C. The lateral size of the crystal domain in the independent $MoS_2$ nanosheets is approximately few nanometers, corresponding to 3–5 layers as seen in Fig. 5b; Fig. 5e shows the SAED of Fig. 5b. These short-range-order structure of $MoS_2$ nanosheets played a number of important roles: (i) the edge-planes of the $MoS_2$ nanosheet structure provided a large number of active sites for redox reactions [12], (ii) the separation and independence of the $MoS_2$ nanosheet allowed the $I_3^-$ ions to easily diffuse to the active sites of the edge-planes for the reduction reaction, and (iii) the independent $MoS_2$ nanosheets increased the specific surface area available to promote the charge-transfer rate. Accordingly, the interlayer distance of the $MoS_2$ nanosheets in this study was about 6 Å; this distance corresponds to the spacing between the (002) basal planes of $MoS_2$, similar to a previous study [15, 45]. Fig. 5c, f show the HRTEM image and SAED of $MoS_x$ annealed at 350 °C, respectively.

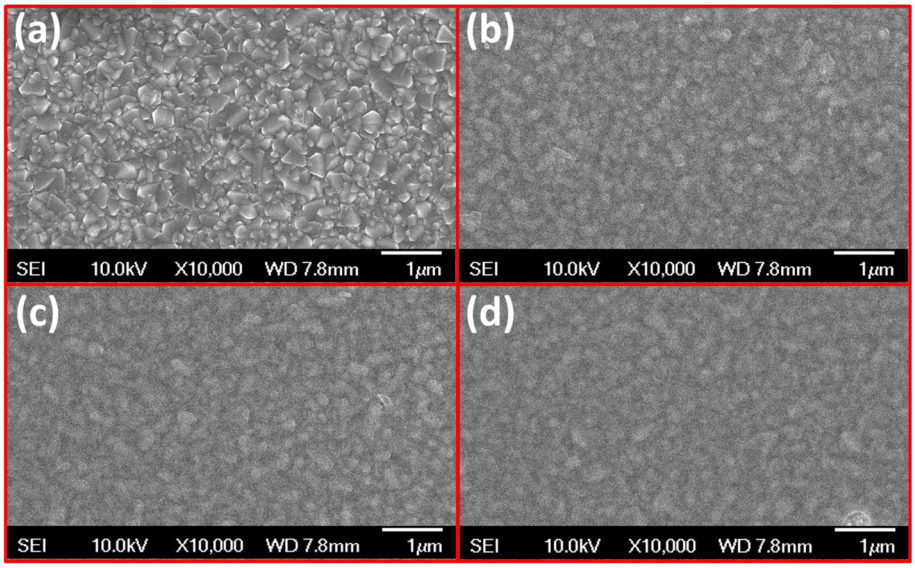


**Fig. 4** The SEM images of the **a** bare FTO and the TR-MoSx samples annealed at **b** 250, **c** 300, and **d** 350 °C, respectively

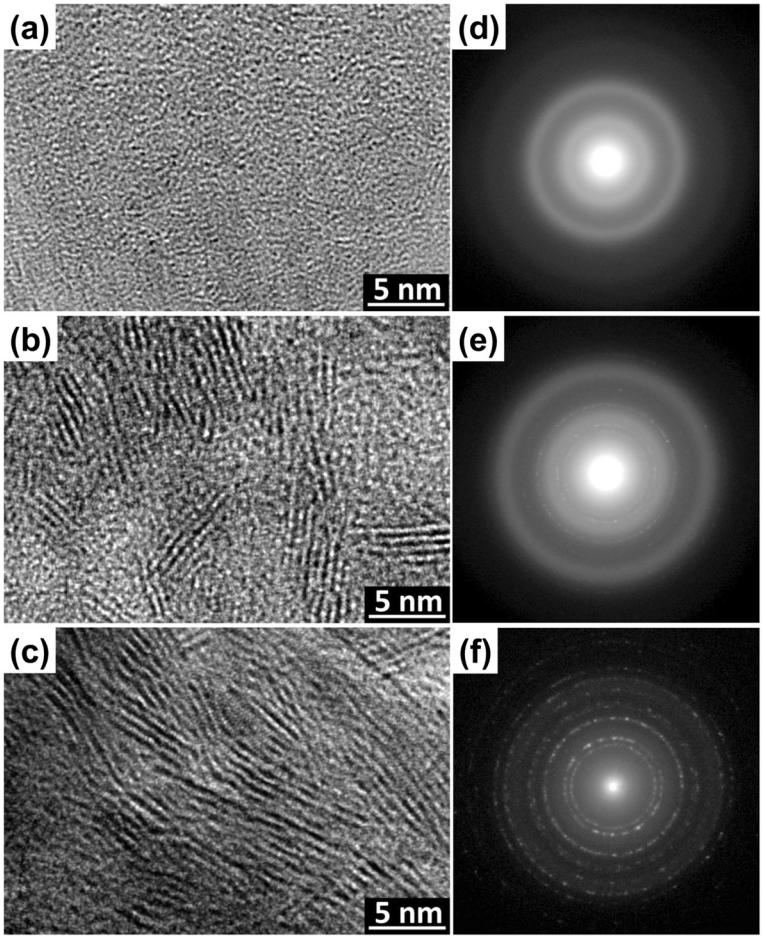


**Fig. 5 a**–**c** TEM images of the TR-$MoS_x$ annealed at 250, 300, and 350 °C and **d**–**f** the corresponding diffraction patterns, respectively

The structure of the $MoS_2$ nanosheets becomes more complete and reduces the number of the edge-planes of the $MoS_2$ nanosheets, as shown in Fig. 5c. Due to this short-range-order structure, fewer edge-planes of active sites can be used in the redox reactions. By comparing Fig. 5f, e with the HRTEM images at different annealing temperatures and their corresponding SAED patterns, we can determine whether the $MoS_2$ crystallization was more complete at higher temperature. To further confirm the identity and structure of the annealed sample, XRD measurements were carried out. Figure 6 shows the XRD pattern of the TR-MoSx samples annealed at 350, 300, and 250 °C, respectively. The diffraction peak (#) of (002) that comes from the basal planes of $MoS_2$ can be observed. On the other hand, compared with the 250 °C annealed sample, the peak intensity and FWHM of $MoS_2$ become more stronger and narrower as the annealing temperature reach to 300 °C; it suggested that the $MoS_2$ crystallization was more complete at higher temperature. From the TEM and XRD results, it is noted that the layered $MoS_2$ nanosheet thin films synthesized on FTO with sulfurization are actually polycrystalline when the annealing temperature exceeds 300 °C; the grain growth occurred at 350 °C to form the long-range-order $MoS_2$ nanosheets.

### Electrocatalytic Properties

In order to estimate the electrocatalytic performance of the TR-$MoS_x$ toward $I_3^-$ reduction, CV analysis was performed using a potential interval ranging from −0.4 to 1.0 vs Ag/AgCl and a scan rate of 50 mV $s^{-1}$. Figure 7a shows the results of the CV measurements in the $I^-/I_3^-$ system based on the TD-Pt CE and TR-$MoS_x$ CEs annealed at 250 °C, 300 °C and 350 °C. Typically, there are two pairs of redox peaks in the cyclic voltammogram. The relatively positive pair (Ox (i) and Red (i)) corresponds to the redox of $I_2/I_3^-$(Eq. (3)). The other pair (Ox (ii) and Red (ii)) is associated with the redox of $I_3^-/I^-$, as presented in Eq. (4).

$$3I_2 + 2e^- = 2I_3^- \quad (3)$$

$$I_3^- + 2e^- = 3I^- \quad (4)$$

The anodic peak current ($I_{pa}$) and the cathodic peak current ($I_{pc}$) corresponded to the oxidation of $I^-$ ions and the reduction of $I_3^-$ ions, respectively. The magnitude of $I_{pc}$ corresponded to the catalytic activation of a C.E. for $I_3^-$ reduction in a DSSC [3]. In addition, the peak to peak voltage separation between the anodic and the cathodic peaks ($E_{pp}$) can be considered to the redox barrier of $I_3^-/I^-$ redox couples. Therefore, the higher $I_{pc}$ and lower $E_{pp}$ values means the better electrocatalytic activity of CEs in DSSC [19]. From Fig. 7 (a), it can be observed that the TD-Pt and TR-$MoS_x$ CEs exhibit two redox pairs, whereas no significant peak is observed when the annealing temperature is below 300 °C. This indicates that our TR-$MoS_x$ annealed at 300 °C exhibits similar electrocatalytic activity to the TD-Pt CE, while the noncrystalline TR-$MoS_x$ CE annealed at 250 °C provides poor electrocatalytic activity. Furthermore, the current density of the redox peaks for the TR-$MoS_x$ CE annealed at 300 °C is higher than those annealed at 250 and 350 °C. In other words, compared to the other conditions, the 300 °C annealed sample can exhibits the highest $I_{pc}$ and lowest $E_{pp}$ that toward the best $I_3^-$ ion electrochemical reduction performance.

To further investigate the electrocatalytic properties, EIS was carried out using symmetrical cells comprising two identical TD-Pt CEs and various TR-$MoS_x$ CEs annealed at 250, 300, and 350 °C, as shown in Fig. 7b. The corresponding EIS parameters obtained from a Nyquist plot are summarized in Table 3, in which $R_s$ corresponds to the series resistance of the electrolyte and electrodes and $R_{ct}$ is the charge-transfer resistance at the electrolyte–electrode interface. From Fig. 7b and Table 3, the $R_{ct}$ values for the TD-Pt CE and the TR-$MoS_x$ CEs annealed at 300 and 350 °C are 14.98, 30.98, and 141.41 Ω $cm^2$, respectively; no $R_{ct}$ value is identified for $MoS_x$ annealed at 250 °C because the $R_{ct}$ was too big to fit. We herein suggest that the noncrystalline $MoS_3$ (annealed at 250 °C) exhibits a poor conductivity due to insufficient energy for sulfidization to produce $MoS_2$, which is consistent with CV results (Fig. 7a).

Tafel polarization measurements were used to examine the exchange current density ($J_0$) at the electrolyte–catalyst interface (shown in Fig. 7c). The tangential slope of the Tafel curve provides information about the exchange current density (linear segments extrapolate to an intercept of log $J_0$), which is closely associated with the $R_{ct}$ value (Eq. (5)) [19]. As we can see in Fig. 7c, the 300 °C

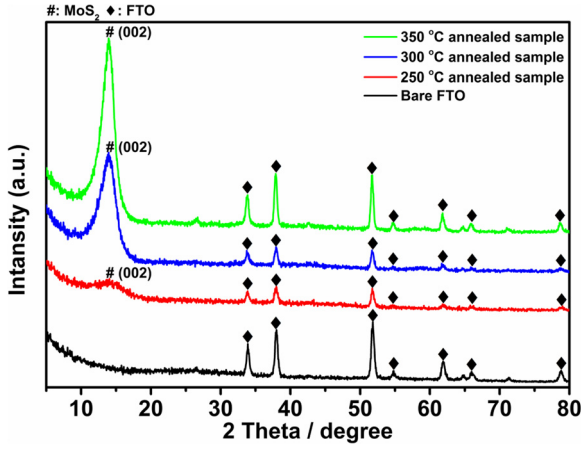


**Fig. 6** The XRD results of the FTO glass and the TR-MoSx samples annealed at 250, 300, and 350 °C, respectively

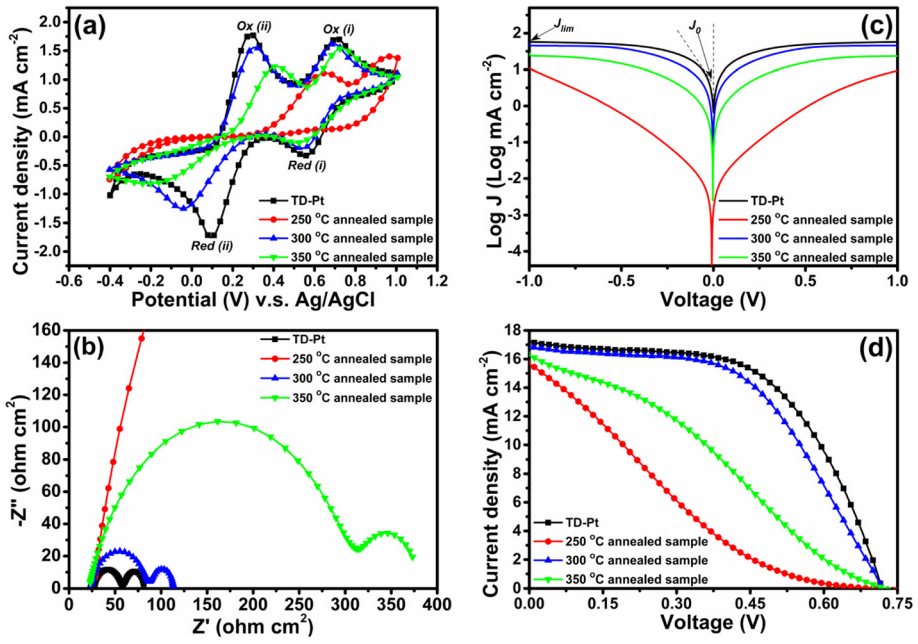


**Fig. 7** Electrocatalytic properties and characterization of the DSSCs assembled with various CEs. **a** CV curves. **b** Nyquist plots. **c** Tafel-polarization curves. and **d** Photocurrent–voltage curves

annealed TR-$MoS_x$ electrode has a large exchange current density ($J_0$) compared with the 250 and the 350 °C annealed samples and was comparable with the TD-Pt electrode (summarized in Table 3), which means higher electrocatalytic activity and lower charge–transfer resistance at the electrolyte–electrode interface.

### Photovoltaic Performance of DSSCs

As shown in Fig. 7d, the photovoltaic performance of DSSCs is characterized using the short-circuit current density ($J_{sc}$), open-circuit voltage ($V_{oc}$), fill factor (FF), and photoconversion efficiency (η); these parameters are summarized in Table 3. The $J_{sc}$, $V_{oc}$, and FF of the DSSC with a reference TD-Pt film CE were 17.056 mA $cm^{-2}$, 0.724 V, and 0.557, respectively, yielding a photoconversion efficiency of 6.929 %. The DSSC with the TR-$MoS_x$ CE annealed at 300 °C exhibits a higher conversion efficiency (6.351 %) compared with those prepared at other annealing temperatures; the corresponding $J_{sc}$, $V_{oc}$, and FF were 16.905 mA $cm^{-2}$, 0.727 V, and 0.517, respectively, which agreed with the CV and EIS measurements. It is worth noting that the values of $J_{sc}$ for the TR-$MoS_2$ CEs annealed at 250 and 350 °C were 15.442 and 16.063 mA $cm^{-2}$, respectively.

As we can see, Tafel-polarization measurements (Fig. 7c) are consistent with the EIS results (showed in Fig. 7b) because $J_0$ is inversely proportional to $R_{ct}$ (Eq. (5)). The lower charge–transfer resistance ($R_{ct}$) at the electrolyte–electrode interface reduces the loss during charge transportation and enhances charge collection efficiency, increasing the photocurrent ($J_{sc}$) and FF of DSSCs.

$$J_0 = \frac{RT}{nFR_{ct}} \tag{5}$$

From Fig. 7c, the TR-$MoS_2$ electrode annealed at 300 °C also possesses the largest limiting current density ($J_{lim}$), which depends on the diffusion

**Table 3** Photovoltaic parameters of the DSSCs based on various CEs and electrochemical parameters from EIS and Tafel measurements

| Counter electrode | $R_s$/Ω $cm^2$ | $R_{ct}$/Ω $cm^2$ | $J_0$/mA $cm^{-2}$ | $J_{sc}$/mA $cm^{-2}$ | $V_{oc}$/V | FF | η(%) |
|---|---|---|---|---|---|---|---|
| TD-Pt film | 27.17 | 14.98 | 4.78 | 17.056 ± 0.075 | 0.724 ± 0.003 | 0.557 ± 0.007 | 6.929 ± 0.063 |
| 250 °C annealed sample | 28.58 | – | 0.01 | 15.442 ± 0.118 | 0.709 ± 0.004 | 0.175 ± 0.002 | 1.917 ± 0.026 |
| 300 °C annealed sample | 23.89 | 30.98 | 2.54 | 16.905 ± 0.013 | 0.727 ± 0.003 | 0.517 ± 0.005 | 6.351 ± 0.045 |
| 350 °C annealed sample | 23.13 | 141.41 | 0.54 | 16.063 ± 0.251 | 0.725 ± 0.005 | 0.299 ± 0.005 | 3.479 ± 0.101 |

coefficient of the $I^-/I_3^-$ redox couple in the DSSC according to Eq. (6) [19].

$$D = \frac{l}{2nFC} J_{\lim} \quad (6)$$

where $R$ is the gas constant, $D$ is the diffusion coefficient of the triiodide, $l$ is the spacer thickness, and $F$ and $n$ have their normal meanings. In other words, EIS and Tafel results explain the good photovoltaic performance of DSSCs based on the TR-$MoS_2$ CE annealed at 300 °C.

The values of $J_{sc}$ and FF can be considered indicative of the number of edge-plane active sites for redox reactions[3]. Although the crystallization of $MoS_2$ was more complete at higher temperature, the $J_{sc}$ and FF of TR-$MoS_x$ annealed at 350 °C ($J_{sc}$ = 16.063, FF = 0.299) are smaller than those of the TR-$MoS_x$ annealed at 300 °C ($J_{sc}$ = 16.905, FF = 0.517). Here, we suggest that the long-range-order nanostructure of the 350 °C annealed $MoS_2$ reduces the active sites of the edge-planes.

In summary, the independent $MoS_2$ nanosheets annealed at 300 °C provide the best electrocatalytic activity toward $I_3^-$ reduction. CV, EIS, and Tafel measurements suggest that the 300 °C annealing temperature should generate a larger active area. This results an excellent photovoltaic conversion efficiency (PCE) of 6.351 % under AM 1.5 illumination of 100 mW $cm^{-2}$, up to 91.7 % of which is obtained using the conventional TD-Pt CE (PCE = 6.929 %). These results demonstrate that the 300 °C annealed TR-$MoS_2$ CE has a great potential as a low-cost alternative to Pt in DSSCs.

## Conclusions

In this work, a two-dimensional nanostructure of $MoS_2$ has been successfully synthesized by a low temperature TR method on FTO glass substrates. This material was also incorporated into a Pt-free DSSC for application. In the TGA results, it was found that the $MoS_2$ sulfidization temperature was approximately 300 °C which provided the effective $MoS_2$ phase transformation process. Additionally, XPS, TEM, and XRD indicate that the stoichiometry and crystallization of $MoS_2$ were more complete at higher temperatures; however, these temperatures reduce the number of edge-plane active sites in the short-range-order nanostructure. The electrochemical analysis also showed that the 300 °C annealed TR-$MoS_2$ CE provided an independent nanosheet nanostructure with numerous active sites that demonstrated Pt-like electrocatalytic activity for $I_3^-$ reduction. These short-range-order nanostructure of $MoS_2$ nanosheets provided a great of edge-plane active sites to enhance the catalytic performance to increase the $J_{sc}$ and *FF*, and an outstanding PCE can be obtained. Accordingly, the DSSC assembled with the 300 °C annealed TR-$MoS_2$ structure exhibited an excellent PCE of 6.351 %; up to 91.7 % of which is obtained using the conventional TD-Pt CE (PCE = 6.929 %). This leads us to the conclusion that the low temperature TR-$MoS_2$ CE is a promising candidate for application as a highly efficient and low-cost CE material in Pt-free DSSCs.

#### Competing Interests

The authors declare that they have no competing interests.

#### Authors' Contributions

CHL designed the methods and experiments, carried out the laboratory experiments, analyzed the data, interpreted the results, and wrote the paper. FGT, CHT, HCW, and CKH worked together on developing the conceptual framework and supervised the work. YYY supported the TGA analysis and discussion. All authors have contributed to the revision of the manuscript and have read and approved the final manuscript.

#### Authors' Information

CHL is PhD program student at National Tsing Hua University. FGT holds a professor position at National Tsing Hua University. CHT holds a professor position at National Tsing Hua University. YYY holds a professor position at Ming Chi University of Technology. HCW holds an associate professor position at Ming Chi University of Technology. CKH holds an assistant professor position at Ming Chi University of Technology.

#### Acknowledgements

The financial support provided by the Ministry of Science and Technology of Taiwan through Project: MOST 103-2221-E-131 -029 is greatly appreciated.

Received: 27 August 2015 Accepted: 11 November 2015
Published online: 17 November 2015

#### References

1. O'Regan B, Gratzel M (1991) A low-cost, high-efficiency solar-cell based on dye-sensitized colloidal TiO2 films. Nature 353:737
2. Gratzel M (2001) Photoelectrochemical cells. Nature 414:338
3. Hsieh CK, Tsai MC, Su CY, Wei SY, Yen MY, Ma CCM et al (2011) A hybrid nanostructure of platinum-nanoparticles/graphitic-nanofibers as a three-dimensional counter electrode in dye-sensitized solar cells. Chem Commun 47:11528
4. Hsieh CK, Tsai MC, Yen MY, Su CY, Chen KF, Ma CCM et al (2012) Direct synthesis of platelet graphitic-nanofibres as a highly porous counter-electrode in dye-sensitized solar cells. Phys Chem Phys 14:4058
5. Chang LH, Hsieh CK, Hsiao MC, Chiang JC, Liu PI, Ho KK et al (2013) A graphene-multi-walled carbon nanotube hybrid supported on oxide as a counter electrode of dye-sensitized solar cells. J Power Sources 222:518
6. Zhang L, Zhang F, Yang X, Long GK, Wu YP, Zhang TF et al (2013) Porous 3D graphene-based bulk materials with exceptional high surface area and excellent conductivity for supercapacitors. Sci Rep 3:1408
7. Hu LH, Wu FY, Lin CT, Khlobystov AN, Li LJ (2013) Graphene-modified LiFePO4 cathode for lithium ion battery beyond theoretical capacity. Nat Commun 4:1687
8. Yoo EZhou HS (2013) Fe phthalocyanine supported by graphene nanosheet as catalyst in Li-air battery with the hybrid electrolyte. J Power Sources 244:429
9. Karunadasa HI, Montalvo E, Sun YJ, Majda M, Long JR, Chang CJ (2012) A molecular MoS2 edge site mimic for catalytic hydrogen generation. Sci 335:698
10. Roy K, Padmanabhan M, Goswami S, Sai TP, Ramalingam G, Raghavan A et al (2013) Graphene-MoS2 hybrid structures for multifunctional photoresponsive memory devices. Nat Nanotechnol 8:826
11. Wang QH, Kalantar-Zadeh K, Kis A, Coleman JN, Strano MS (2012) Electronics and optoelectronics of two-dimensional transition metal dichalcogenides. Nat Nanotechnol 7:699
12. Kibsgaard J, Chen ZB, Reinecke BN, Jaramillo TF (2012) Engineering the surface structure of MoS2 to preferentially expose active edge sites for electrocatalysis. Nat Mater 11:963

13. Pham VH, Kim KH, Jung DW, Singh K, Oh ES, Chung JS (2013) Liquid phase co-exfoliated MoS2-graphene composites as anode materials for lithium ion batteries. J Power Sources 244:280
14. Yang LC, Wang SN, Mao JJ, Deng JW, Gao QS, Tang YSchmidt OG (2013) Hierarchical MoS2/polyaniline nanowires with excellent electrochemical performance for lithium-ion batteries. Adv Mater 25:1180
15. Sun PL, Zhang WX, Hu XL, Yuan LX, Huang YH (2014) Synthesis of hierarchical MoS2 and its electrochemical performance as an anode material for lithium-ion batteries. J Mater Chem A 2:3498
16. Firmiano EGS, Cordeiro MAL, Rabelo AC, Dalmaschio CJ, Pinheiro AN, Pereira EC et al (2012) Graphene oxide as a highly selective substrate to synthesize a layered MoS2 hybrid electrocatalyst. Chem Commun 48:7687
17. Jaramillo TF, Jorgensen KP, Bonde J, Nielsen JH, Horch SChorkendorff I (2007) Identification of active edge sites for electrochemical H-2 evolution from MoS2 nanocatalysts. Science 317:100
18. Tai SY, Liu CJ, Chou SW, Chien FSS, Lin JY, Lin TW (2012) Few-layer MoS2 nanosheets coated onto multi-walled carbon nanotubes as a low-cost and highly electrocatalytic counter electrode for dye-sensitized solar cells. J Mater Chem 22:24753
19. Al-Mamun M, Zhang HM, Liu PR, Wang Y, Cao HJ, Zhao J (2014) Directly hydrothermal growth of ultrathin MoS2 nanostructured films as high performance counter electrodes for dye-sensitised solar cells. Rsc Adv 4:21277
20. Benavente E, Santa Ana MA, Mendizabal G, Gonzalez F (2002) Intercalation chemistry of molybdenum disulfide. Coordin Chem Rev 224:87
21. Seayad A, MAntonelli DM (2004) Recent advances in hydrogen storage in metal-containing inorganic nanostructures and related materials. Adv Mater 16:765
22. Matte HSSR, Gomathi A, Manna AK, Late DJ, Datta R, Pati SK et al (2010) MoS2 and WS2 analogues of graphene. Angew Chem Int Edit 49:4059
23. Shi YM, Zhou W, Lu AY, Fang WJ, Lee YH, Hsu AL et al (2012) van der Waals epitaxy of MoS2 layers using graphene as growth templates. Nano Lett 12:2784
24. Radisavljevic B, Radenovic A, Brivio J, Giacometti V, Kis A (2011) Single-layer MoS2 transistors. Nat Nanotechnol 6:147
25. Zhou KG, Mao NN, Wang HX, Peng Y, Zhang HL (2011) A mixed-solvent strategy for efficient exfoliation of inorganic graphene analogues. Angew Chem Int Edit 50:10839
26. Tang ZH, Wei QY, Guo BC (2014) A generic solvent exchange method to disperse MoS2 in organic solvents to ease the solution process. Chem Commun 50:3934
27. Wang YC, Ou JZ, Balendhran S, Chrimes AF, Mortazavi M, Yao DD et al (2013) Electrochemical control of photoluminescence in two-dimensional MoS2 nanoflakes. Acs Nano 7:10083
28. Coleman JN, Lotya M, O'Neill A, Bergin SD, King PJ, Khan U et al (2011) Two-dimensional nanosheets produced by liquid exfoliation of layered materials. Sci 331:568
29. Huang GC, Chen T, Chen WX, Wang Z, Chang K, Ma L et al (2013) Graphene-like MoS2/graphene composites: cationic surfactant-assisted hydrothermal synthesis and electrochemical reversible storage of lithium. Small 9:3693
30. Lauritsen JV, Kibsgaard J, Helveg S, Topsoe H, Clausen BS, Laegsgaard E et al (2007) Size-dependent structure of MoS2 nanocrystals. Nat Nanotechnol 2:53
31. Helveg S, Lauritsen JV, Laegsgaard E, Stensgaard I, Norskov JK, Clausen BS et al (2000) Atomic-scale structure of single-layer MoS2 nanoclusters. Phys Rev Lett 84:951
32. Liu KK, Zhang WJ, Lee YH, Lin YC, Chang MT, Su C et al (2012) Growth of large-area and highly crystalline MoS2 thin layers on insulating substrates. Nano Lett 12:1538
33. Lee YH, Zhang XQ, Zhang WJ, Chang MT, Lin CT, Chang KD et al (2012) Synthesis of large-area MoS2 atomic layers with chemical vapor deposition. Adv Mater 24:2320
34. Shi ZW, Lu H, Liu Q, Cao FR, Guo J, Deng KM et al (2014) Efficient p-type dye-sensitized solar cells with all-nano-electrodes: NiCo2S4 mesoporous nanosheet counter electrodes directly converted from NiCo2O4 photocathodes. Nanoscale Res Lett 9:608
35. Manikandan A, Saravanan A, Antony SA, Bououdina M (2015) One-pot low temperature synthesis and characterization studies of nanocrystalline alpha-Fe2O3 based dye sensitized solar cells. J Nanosci Nanotechno 15:4358
36. Kong DS, Wang HT, Cha JJ, Pasta M, Koski KJ, Yao J et al (2013) Synthesis of MoS2 and MoSe2 films with vertically aligned layers. Nano Lett 13:1341
37. Lim J, Kim HA, Kim BH, Han CH, Jun Y (2014) Reversely fabricated dye-sensitized solar cells. Rsc Adv 4:243
38. Brito JL, Ilija M, Hernandez P (1995) Thermal and reductive decomposition of ammonium thiomolybdates. Thermochim Acta 256:325
39. Dungey KE, Curtis MD, Penner-Hahn JE (1998) Structural characterization and thermal stability of MoS2 intercalation compounds. Chem Mater 10:2152
40. Wang HW, Skeldon P, Thompson GE (1997) XPS studies of MoS2 formation from ammonium tetrathiomolybdate solutions. Surf Coat Tech 91:200
41. Liu CJ, Tai SY, Chou SW, Yu YC, Chang KD, Wang S et al (2012) Facile synthesis of MoS2/graphene nanocomposite with high catalytic activity toward triiodide reduction in dye-sensitized solar cells. J Mater Chem 22:21057
42. Wang HW, Skeldon P, Thompson GE, Wood GC (1997) Synthesis and characterization of molybdenum disulphide formed from ammonium tetrathiomolybdate. J Mater Sci 32:497
43. Weber T, Muijsers JC, Niemantsverdriet JW (1995) Structure of amorphous Mos3. J Phys Chem-Us 99:9194
44. Gao DQ, Si MS, Li JY, Zhang J, Zhang ZP, Yang ZL et al (2013) Ferromagnetism in freestanding MoS2 nanosheets. Nanoscale Res Lett 8:129
45. Najmaei S, Liu Z, Ajayan PM, Lou J (2012) Thermal effects on the characteristic Raman spectrum of molybdenum disulfide (MoS2) of varying thicknesses. Appl Phys Lett 100:013106